Applied Catalysis B: Environmental 182 (2016) 356–368

Contents lists available at ScienceDirect

Applied Catalysis B: Environmental

journal homepage: www.elsevier.com/locate/apcatb

# Selective oxidation of aromatic alcohols to aromatic aldehydes by BN/metal sulfide with enhanced photocatalytic activity

Sugang Meng[a], Xiangju Ye[b], Xiaofeng Ning[a], Mengli Xie[a], Xianliang Fu[a], Shifu Chen[a,b,*]

[a] Department of Chemistry, Huaibei Normal University, Anhui Huaibei 235000, People's Republic of China
[b] Department of Chemistry, Anhui Science and Technology University, Anhui Fengyang 233100, People's Republic of China

ARTICLE INFO

*Article history:*
Received 4 July 2015
Received in revised form
13 September 2015
Accepted 15 September 2015
Available online 21 September 2015

*Keywords:*
Selective oxidation
Aromatic alcohols
BN nanosheets
$In_2S_3$
Visible light

ABSTRACT

BN/metal sulfide composite (BN/$In_2S_3$) was prepared by a facile in situ one-pot hydrothermal method. The as-synthesized photocatalyst was characterized by X-ray powder diffraction (XRD), UV–vis diffuse reflection spectroscopy (DRS), scanning electron microscopy (SEM), transmission electron microscopy (TEM), $N_2$-sorption analysis, electron spin resonance (ESR), photoluminescence emission spectra (PL) and X-ray photoelectron spectroscopy (XPS). The results show that compared with single $In_2S_3$, the BN/$In_2S_3$ photocatalyst exhibits excellent photocatalytic performance for selective oxidation of aromatic alcohols to aromatic aldehydes under visible light irradiation. The enhanced photocatalytic activity of BN/$In_2S_3$ composite is mainly attributed to the unique physicochemical properties of BN nanosheet, which acts as a promoter for photoexcited holes transfer, thereby improving the charge separation efficiency and prolonging photoexcited electrons lifetime. Effects of the type of aromatic alcohol and the added scavenger on the photocatalytic efficiency were also investigated. $^{\bullet}O_2^-$ radicals and photogenerated holes play decisive roles for photocatalytic oxidation of aromatic alcohols to aromatic aldehydes. This approach is versatile for constructing other high efficiency photocatalysts such as BN/CdS, BN/$Cd_xZn_{1-x}S$ and BN/$ZnIn_2S_4$. It is hoped that this work could provide new insights to construct the BN-based composites for extensive photocatalytic applications.



## 1. Introduction

The partial oxidation of aromatic alcohol to corresponding aldehyde is a useful and fundamental organic reaction, because such aromatic aldehydes and their derivatives are important building blocks for the synthesis of fine chemicals and pharmaceuticals [1]. Traditionally, this reaction system is carried out using dioxygen in lieu of toxic or corrosive stoichiometric oxidants such as hypochlorite, chromate, and chlorine [2]. However, the methods produce large amounts of wastes during the reaction process [3]. Therefore, it is urgent and necessary to develop a cost-efficient and environmentally friendly method for selective oxidation of aromatic alcohol to corresponding aldehydes under mild conditions.

In the past decades, the semiconductor photocatalysis has attracted scientists' extensive research interest because it can be applied to solar energy utilization [4,5], environmental remediation [6], and selective transformation of organic compounds [7], etc. [8]. Generally, $TiO_2$ is considered to be one of the most promising photocatalysts because of its high catalytic activity, the physical and chemical stability, non-toxic and low cost [5]. It has been reported that $TiO_2$ can be used in the degradation of environmental pollutants, hydrogen production via photolysis of water and selective transformation of organic compounds, especially for the selective oxidation of alcohols to corresponding aldehydes [9,10]. However, $TiO_2$ only makes use of part of sunlight due to its width of band gap (3.2 eV). Furthermore, because the valence band (VB) position of $TiO_2$ is about 2.7 eV, the powerful oxidizing capacity of photoexcited holes will weaken its selectivity. For example, Yurdakal et al. prepared a series of $TiO_2$ samples and used them in performing the partial oxidation of benzyl alcohol to benzaldehyde under UV–vis light irradiation. The highest selectivity value obtained by these photocatalysts was about 38.2% [10(a)]. This was because, besides benzaldehyde, benzoic acid and carbon dioxide were also indiscriminatingly produced in the process of photocatalytic reaction. Therefore, in order to improve the photocatalytic performance of $TiO_2$ for the selective oxidation of alcohols to aldehydes, the modification of $TiO_2$ through doping noble metals [11] and ions [12], or coupling with different semiconductors have been extensively investigated [13]. The results showed that the selectivity was obviously enhanced. At the same time, non-$TiO_2$ photocatalysts

* Corresponding author. Fax: +86 550 6732001.
*E-mail address:* chshifu@chnu.edu.cn (S. Chen).

http://dx.doi.org/10.1016/j.apcatb.2015.09.030
0926-3373/

used for the selective oxidation of alcohols to aldehydes were also investigated, such as $CeO_2$ [14], $C_3N_3S_3$ [15], $C_3N_4$ [16], CdS [17], $ZnIn_2S_4$ [18], $In_2S_3$ [19], etc. [20]. Among these, metal sulfides attract more attention because of unique photoelectrochemical properties and high photocatalytic performance [17–20]. For example, CdS was used as a photocatalyst for the selectivity of benzyl alcohol to benzaldehyde, the selectivity was about 90% under visible light irradiation for 3 h [17(b)]. For $In_2S_3$ photocatalyst, the selectivity was 99.8% under visible light illuminated for 4 h [19]. Meanwhile, metal sulfides are easily controlled and combined with other materials for promoting its photocatalytic performance. For example, Xu's group reported that the graphene-supported metal sulfide (CdS [17], $ZnIn_2S_4$ [18], and $In_2S_3$ [21]) composites were used for the photocatalytic selective organic synthesis. The result showed that when CdS was coupled with 5% graphene, the selectivity of the photocatalyst could reach 100% [17(b)] Here, graphene is used as an electron-transferrer for facilitating the separation of photoexcited electron-hole pairs and consequently improving its photocatalytic activities. It is known that when a photocatalyst is photoexcited, holes accompanying electrons will also be generated. Therefore, if there is a hole-capturer coupled with metal sulfide photocatalyst, the photocatalytic activity of metal sulfide would also be enhanced.

Hexagonal boron nitride (BN) is a kind of metal-free material, which is similar to layered-structure graphene and has unique physicochemical properties, such as low density, high stability and thermal conductivity [22]. More importantly, BN will be electronegative when the bulk BN was exfoliated into two-demension (2D) nanosheets [23,24]; the negatively charged BN nanosheets will attract the photoexcited holes and promote the separation efficiency of photoexcited electron-hole pairs. Theoretical and experimental work has confirmed that the negatively charged BN derives from stable defects associated with nitrogen vacancies (N edged triangle defects) or carbon impurities [23,24]. Because the reconstruction of BN by ball milling process has been investigated by our previous study [23] and no carbon impurities was involved in the milling process, the negative charge of BN nanosheets is more likely originated from the nitrogen vacancies formed during the process. Therefore, compared with pure metal sulfides, the BN/metal sulfides composite will enhance the photocatalytic activity greatly. However, to the best of our knowledge, BN/metal sulfide formed by metal sulfide coupled with 2D BN nanosheets for improving the activity of selective oxidation of aromatic alcohols to corresponding aromatic aldehydes has not been reported up to now.

In this paper, BN/$In_2S_3$ composite was prepared firstly by a one-step hydrothermal method. The physical, chemical and optical properties of the resulted samples were thoroughly characterized with XRD, UV–vis DRS, BET, SEM, TEM, PL, ESR, XPS and so on. The photocatalytic performance of BN/$In_2S_3$ composite was investigated by determining the conversion and selectivity of benzyl alcohol to benzaldehyde. The probable reaction mechanism for selective oxidation of aromatic alcohols to aromatic aldehydes was proposed. This approach is versatile for the application of other BN/metal sulfide composites, such as BN/CdS, BN/$Cd_xZn_{1-x}S$ and BN/$ZnIn_2S_4$.

## 2. Experimental

### 2.1. Materials

5, 5-dimethyl-1-pyrroline-N-oxide (DMPO) was obtained from Sigma Co. Negatively charged BN nanosheets were prepared by ball milling method in our previous paper [23]. Indium chloride tetrahydrate ($InCl_3{\cdot}4H_2O$), thiacetamide (TAA), hydrochloric acid (HCl), benzyl alcohol, benzaldehyde and other chemicals used in the experiments are of analytical reagent grade and were supplied by Shanghai Chemical Reagent Co. Ltd of China. Deionized water was used throughout this study.

### 2.2. Preparation of photocatalysts

BN/$In_2S_3$ composite was synthesized by a simple hydrothermal method. Typically, a certain amount of BN nanosheets were dispersed in the deionized water. 1.0 mmol $InCl_3{\cdot}4H_2O$ was dissolved in the above BN suspension. And then, 2.5 mmol TAA as the source of sulfur was added into the above solution. The pH was adjusted to 3 by dropwising HCl by continuous magnetic stirring. The obtained suspension was transferred into a 100 mL teflon-lined stainless steel autoclave, and then was heated to 180 °C for 24 h. After cooling down to room temperature naturally, the orange products were collected and washed by deionized water and absolute ethyl alcohol for 3 times, respectively. Finally, the obtained products were dried in air at 60 °C.

To illustrate the role of BN nanosheet for improving photocatalytic activity in BN/metal sulfide composite, other BN/metal sulfides (BN/$ZnIn_2S_4$, BN/$Cd_xZn_{1-x}S$ and BN/CdS) were also prepared by the above hydrothermal method. Synthesis of BN/$ZnIn_2S_4$, 1 mmol $ZnCl_2$ and 2 mmol $InCl_3{\cdot}4H_2O$ were dissolved in 75 mL of BN suspension and stirred for 60 min, and then 6 mmol TAA were added into the reaction system and the pH was adjusted to 2.5 by hydrochloric acid. The mixture was transferred into a 100 mL teflon-lined stainless steel autoclave, and then was heated to 140 °C for 12 h. Synthesis of BN/$Cd_xZn_{1-x}S$, 3 mmol $Cd(Ac)_2{\cdot}2H_2O$ and 1 mmol $Zn(Ac)_2{\cdot}2H_2O$ were dissolved in 75 mL of BN suspension and stirred for 60 min, and then 4 mmol thiourea was added into the reaction system. After 60 min of continuous stirring, the obtained suspension was transferred into a 100 mL teflon-lined stainless steel autoclave and maintained at 180 °C for 12 h. Synthesis of BN/CdS, 2 mmol $Cd(NO_3)_2{\cdot}4H_2O$ was dissolved in 75 mL of BN suspension and stirred for 60 min. Then 4 mmol TAA were added into the reaction system. After 60 min of continuous stirring, the obtained suspension was transferred into a 100 mL teflon-lined stainless steel autoclave, and then was heated to 180 °C for 12 h. For comparison, the pure $In_2S_3$, $ZnIn_2S_4$, $Cd_xZn_{1-x}S$ and CdS were also synthesized by the same hydrothermal method except for absence of BN.

### 2.3. Characterization

In order to determine the crystal phase composition and the crystallite size of the photocatalysts, X-ray diffraction (XRD) measurement was carried out at room temperature using a Bruker D8 advance X-ray powder diffractometer with Cu Kα radiation and a scanning speed of 3°/min. The crystallite size was calculated by X-ray line broadening analysis using the Scherrer equation. The accelerating voltage and emission current were 40 kV and 40 mA, respectively. UV–vis diffuse reflectance spectroscopy (DRS) measurements were carried out using a Hitachi UV-365 spectrophotometer equipped with an integrating sphere attachment. $BaSO_4$ was used as a reflectance standard. The microcrystalline structure and surface characteristics of the photocatalyst were investigated using (JEOL JSM-6610LV) scanning electron microscope (SEM). Transmission electron microscopy (TEM) and high-resolution transmission electron microscopy (HR-TEM) images were performed with a JEOL-2010 transmission electron microscope, using an accelerating voltage of 200 kV. The Brunauer–Emmett–Teller (BET) surface areas were detected by a Micromeritics ASAP 2020. Photoluminescence emission spectra (PL) were recorded on a JASCO FP-6500 type fluorescence spectrophotometer with an excitation wavelength of 420 nm. Electron

spin resonance (ESR) signals of spin-trapped paramagnetic species with 5, 5-dimethyl-l-pyrroline N-oxide (DMPO) were detected using a Bruker A300E spectrometer under visible light irradiation ($\lambda > 420$ nm).

The photoelectrochemical experiments were performed in a three-electrode system (CHI-660D, Chenhua Instruments Co., Shanghai, China). A Pt wire and Ag/AgCl were used as counter electrode and reference electrode, respectively. The catalyst powder was deposited on the fluoride tin oxide (FTO) substrate to serve as the working electrode. A quartz cell ($50 \times 50 \times 55$ mm) filled with 0.1 M $Na_2SO_4$ or 0.1 M KCl electrolyte was used as the reaction system. A 300 W Xenon lamp (PLS-SXE 300C, Beijing Perfect light) equipped with a 420 nm cutoff filter ($\lambda > 420$ nm) was applied as a visible light source.

### 2.4. Evaluation of photocatalytic activity

The photocatalytic selective oxidation of aromatic alcohols to corresponding aromatic aldehydes was performed as follows. A mixture of alcohol (0.5 mmol) and 80 mg of photocatalyst was dispersed in the inert solvent of 15 mL benzotrifluoride (BTF). It was chosen as a solvent due to BTF's nonreactivity and high solubility for molecular oxygen [25]. The prepared solution was loaded into a 100 mL of Teflon-lined stainless steel autoclave with a pressure gage which can be very convenient for monitoring the pressure in the autoclave. The illumination window on the top of the reactor is made of high strength quartz glass. Before the reaction, the autoclave was filled with molecular oxygen at a pressure of 0.1 Mpa, and the suspension was magnetically stirred for 30 min to reach adsorption–desorption equilibrium. A 300 W Xenon lamp (PLS-SXE 300C, Beijing Perfect light) with a maximum emission at about 470 nm was used as a visible light source. The wavelength of the visible light was controlled through a 420 nm cutoff filter ($\lambda > 420$ nm, Instrument Company of Nantong, China). After the reaction, the mixture was centrifuged to remove the photocatalyst particles. The obtained solution was analyzed by a Gas Chromatograph (FuLi-9790) equipped with a SE-30 capillary column (30 m, 0.53 mm, Lanzhou Atech Technologies Co. Ltd). Conversion of alcohol, yield of aldehyde, and selectivity for aldehyde were defined as the follows:

$$\text{Conversion}(\%) = \left[\frac{(C_0 - C_{\text{alcohol}})}{C_0}\right] \times 100 \quad (1)$$

$$\text{Yield}(\%) = \frac{C_{\text{aldehyde}}}{C_0} \times 100 \quad (2)$$

$$\text{Selectively}(\%) = \left[\frac{C_{\text{aldehyde}}}{(C_0 - C_{\text{alcohol}})}\right] \times 100 \quad (3)$$

where $C_0$ is the initial concentration of alcohol; $C_{\text{alcohol}}$ and $C_{\text{aldehyde}}$ are the concentration of the substrate alcohol and the corresponding aldehyde at a certain time after the photocatalytic reaction, respectively.

## 3. Results and discussion

### 3.1. Characterization of BN/$In_2S_3$ composite

#### 3.1.1. XRD analysis

The crystallographic structure and phase composition of BN, BN/$In_2S_3$ and $In_2S_3$ are displayed in Fig. 1. The diffraction peaks of BN can be indexed to hexagonal BN (JCPDS 73-2095). One main diffraction peak of BN located at 2θ values of 26.9° is assigned to (0 0 2) crystallographic plane [23]. The as-synthesized BN/$In_2S_3$ composites with different weight ratios of BN exhibit similar XRD patterns to the pure $In_2S_3$. The peaks located at about 14.2, 23.3, 27.4, 28.7, 33.4, 43.6, 47.8, 50.1, 55.9, 56.6, 59.5, 66.8, 69.9 and 76.9° are distinctly indexed to the (1 1 1), (2 2 0), (3 1 1), (2 2 2), (4 0 0), (5 1 1), (4 4 0), (5 3 1), (5 3 3), (6 2 2), (4 4 4), (7 3 1), (8 0 0) and (7 5 1) crystal planes of pure cubic $In_2S_3$ phase (JCPDS No.65-0459), respectively. However, no peaks for BN can be found in the BN/$In_2S_3$ composites when the weight ratio of BN is lower than 10%. It may be due to the low amount of BN in the BN/$In_2S_3$ composite, and the guest BN nanosheet is covered with a large amount of host $In_2S_3$ sample. The peak for BN located at 26.9° can be observed when BN loading amount is higher than 10%. No other peaks were detected in the XRD patterns, demonstrating that no new species or impurities were formed in the hydrothermal process. In addition, the main peaks of BN, BN/$In_2S_3$ and $In_2S_3$ samples are all very sharp, indicating good crystallinity. The average crystallite sizes of $In_2S_3$ nanoparticles are calculated from the (4 4 0) peak of the XRD patterns by the Scherrer formula: $D = 0.89\lambda/B\cos\theta$, where D, λ, B and θ are the average crystallite size, the Cu Kα wavelength, the half-width of the main peak and the corresponding diffraction angle, respectively [21,26]. The average crystallite sizes of $In_2S_3$ nanoparticles in the pure $In_2S_3$, 3% BN/$In_2S_3$, 5% BN/$In_2S_3$, 7% BN/$In_2S_3$, 10% BN/$In_2S_3$ and 20% BN/$In_2S_3$ composites are about 19.3, 20.2, 19.3, 20.5, 20.8 and 19.9 nm, respectively. It is obvious that their average crystallite sizes are close to each other, indicating that the presence of BN does not influence the crystallite structure and size of $In_2S_3$.

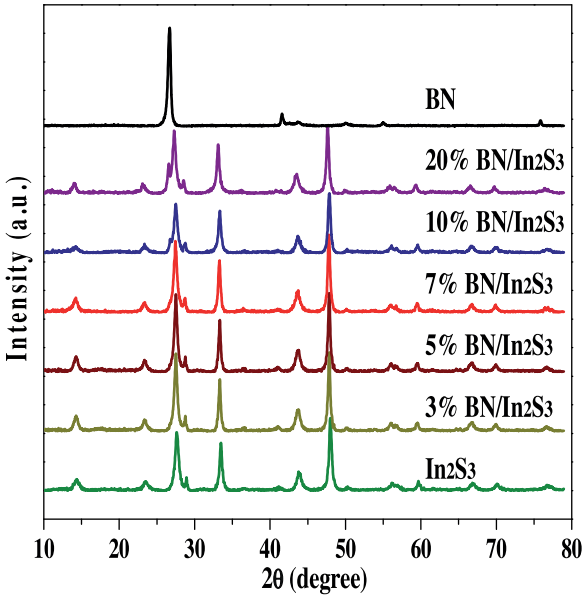


**Fig. 1.** XRD patterns of pure $In_2S_3$, BN, and BN/$In_2S_3$ composites.

#### 3.1.2. UV–vis DRS analysis

UV–vis diffuse reflection spectra are used to detect the optical properties of the as-synthesized samples. As shown in Fig. 2a, it is clear that BN shows a low visible light absorption because its intrinsic absorption is located at about 210 nm [23]. However, $In_2S_3$ exhibits strong absorption in the visible region from 400 to 630 nm, and BN/$In_2S_3$ composites display almost the same optical absorption as that of $In_2S_3$. Moreover, the band gap energy (Eg) of the $In_2S_3$ sample is calculated by the following equation: $\alpha h\nu = A(h\nu - Eg)^{1/2}$. Where α, A, h and v are absorption coefficient, proportionality, Planck constant and light frequency, respectively [27]. As shown in Fig. 2b, the band gap of the pure $In_2S_3$ is about 1.95 eV. For BN/$In_2S_3$ composites with different loading amount of BN, their band gap energies do not have obvious deviation compared with pure $In_2S_3$ sample, suggesting the optical property of $In_2S_3$ is not obviously changed by addition of BN. It is mainly because hexagonal-BN nanosheets possess high transmission within visible light region

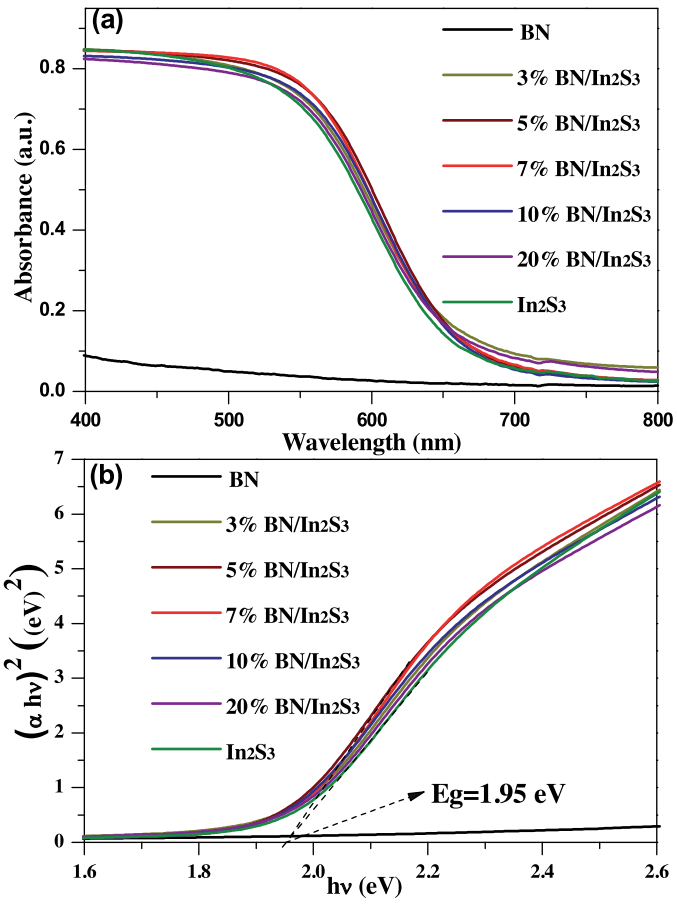


**Fig. 2.** (a) UV–vis diffuse reflectance spectra (DRS) and (b) band gap energies of pure $In_2S_3$, BN, and BN/$In_2S_3$ composites.

[22,23]. The results are in accordance with our previous reports [19,23].

### 3.1.3. SEM and TEM analysis

In order to investigate the morphology and analyze the effect of the BN nanosheets on the microscopic structure of the BN/$In_2S_3$ composites, SEM and TEM analysis were performed. Fig. 3 shows SEM images of $In_2S_3$ and 7% BN/$In_2S_3$. It can be seen that the pure $In_2S_3$ exhibits spherical-like shape (Fig. 3a), which is composed of a large quantity of aggregated nano-fragments (Fig. 3b). The thickness of the nano-fragments is less than 10 nm. These nano-fragments construct the spherical-like surface of $In_2S_3$, which is analogous to the hierarchical structure [21]. When BN nanosheets were added into the reaction system, as can be seen form Fig. 3c–d, the morphology of 7% BN/$In_2S_3$ has no obvious change. However, there are some small nano-fragments coupled on the surface of the bigger nano-fragments, and the thickness of the BN/$In_2S_3$ nanosheets (>10 nm) is greater than that of $In_2S_3$. These reflect the good interfacial contact between $In_2S_3$ nano-fragments and BN nanosheets. TEM was used to further investigate the microscopic morphology and structure of the sample. It can be seen that ultrathin BN nanosheets are mono-dispersed with diameter of 50–150 nm (Fig. 4a). The energy dispersive X-ray spectroscopy (EDX) (Fig. 4b) reveals that the sample is composed of boron (B) and nitrogen (N), and carbon (C), oxygen (O) and copper (Cu) come from the carbon membrane and copper wire mesh. Fig. 4c shows that $In_2S_3$ nano-fragments are uniformly deposited onto the smooth surfaces of the ultrathin BN nanosheets. Fig. 4d displays the HR-TEM image of the BN/$In_2S_3$ composite. It exhibits distinct lattice fringes with 0.32 nm, which can be ascribed to the (3 1 1) crystallographic plane of $In_2S_3$. Moreover, the EDX pattern of BN/$In_2S_3$ composite indicates that the sample is composed of B, N, In and S elements (Fig. 4b).

### 3.1.4. XPS analysis

To study the surface compositions and chemical state of the as-prepared BN/$In_2S_3$ composites, XPS measurements were carried out. The survey spectrum of BN/$In_2S_3$ is shown in Fig. 5a. It reveals that no peaks of other elements except In, S, B, N, C and O are observed. The peaks of C and O probably come from the absorbed gaseous molecules or the graphite conductive adhesive. High resolution core spectra for In 3d, S 2p are displayed in Fig. 5b and c. The peaks at the binding energy of 444.6 and 452.1 eV are attributed to In $3d_{5/2}$ and In $3d_{3/2}$, while the peaks at 161.4 and 162.6 eV could be attributed to S $2p_{3/2}$ and S $2p_{1/2}$ transition, respectively [28]. The In and S spin orbit separations are found to be 7.5 and 1.2 eV, and the ratios of two peaks are about 2:3 and 1:2. These results indicate that In and S are present as $In^{3+}$ and $S^{2-}$ in the BN/$In_2S_3$ composite. The XPS spectra of B and N are shown in Fig. 5d and e. Their binding energies are 189.8 and 397.4 eV, respectively. Moreover, the atomic percents of B and N in the sample are about 24.38% and 24.6%, respectively (it is determined by internal standard method with the aid of relative sensitivity factors). It is clear that the atomic number ratio of B and N is about 1:1. XPS spectra of pure $In_2S_3$ and BN for In 3d, S 2p, B 1s, and N 1s are shown in Fig. 5. It is clear that In 3d and S 2p XPS spectra of pure $In_2S_3$ show no obvious change compared with the XPS spectra of BN/$In_2S_3$. The B 1s and N 1s XPS spectra of pure BN are also similar with that of the BN/$In_2S_3$. It indicates that there is no obvious chemical bond connection between BN and $In_2S_3$.

Based on the results of above characterizations, it is suggested that BN/$In_2S_3$ composites with a good interfacial contacts have been readily achieved via a one-step hydrothermal method. It is reasonably speculated that these BN/$In_2S_3$ samples will exhibit excellent applications in photocatalytic selective organic transformation under mild conditions.

### 3.1.5. BET analysis

Fig. 6 displays the nitrogen adsorption–desorption isotherms of pure BN nanosheets, $In_2S_3$ and 7% BN/$In_2S_3$ composite, respectively. It is clear that these samples show type IV isotherms, implying the samples have porous structure as a result of the accumulation of the nanosheets (Fig. 3). The BET surface areas of BN, $In_2S_3$ and 7% BN/$In_2S_3$ composite are about 27.2, 28.3 and 27.4 $m^2/g$, respectively.

## 3.2. Evaluation of photocatalytic activities

### 3.2.1. Selective oxidation of benzyl alcohol to benzaldehyde

The photocatalytic activity of BN/$In_2S_3$ composite is initially tested by selective oxidation of benzyl alcohol to benzaldehyde in benzotrifluoride under visible light irradiation for 3 h. As shown in Fig. 7, the conversion of benzyl alcohol increases constantly with the increase of content of BN; however, when the content of BN is higher than 7%, the conversion of benzyl alcohol begins to reduce with the increase of amount of BN. This may be attributed to the fact that the introduction of excessive BN nanosheets could inhibit visible light absorption (as shown in Fig. 2a, 7% BN/$In_2S_3$ showed the highest absorption than that of other BN/$In_2S_3$ in the wavelength range of 400–600 nm) and shield the active sites on the surface of the spherical-like $In_2S_3$ (as shown in Fig. 4c, $In_2S_3$ nano-fragments were uniformly deposited onto the surface of the BN nanosheets when the amount of BN is 7%). Thus, it can be seen that the combination of BN with $In_2S_3$ has an important influence on the photocatalytic performance of the samples. The result is similar to the previous reports that a suitable loading amount is crucial

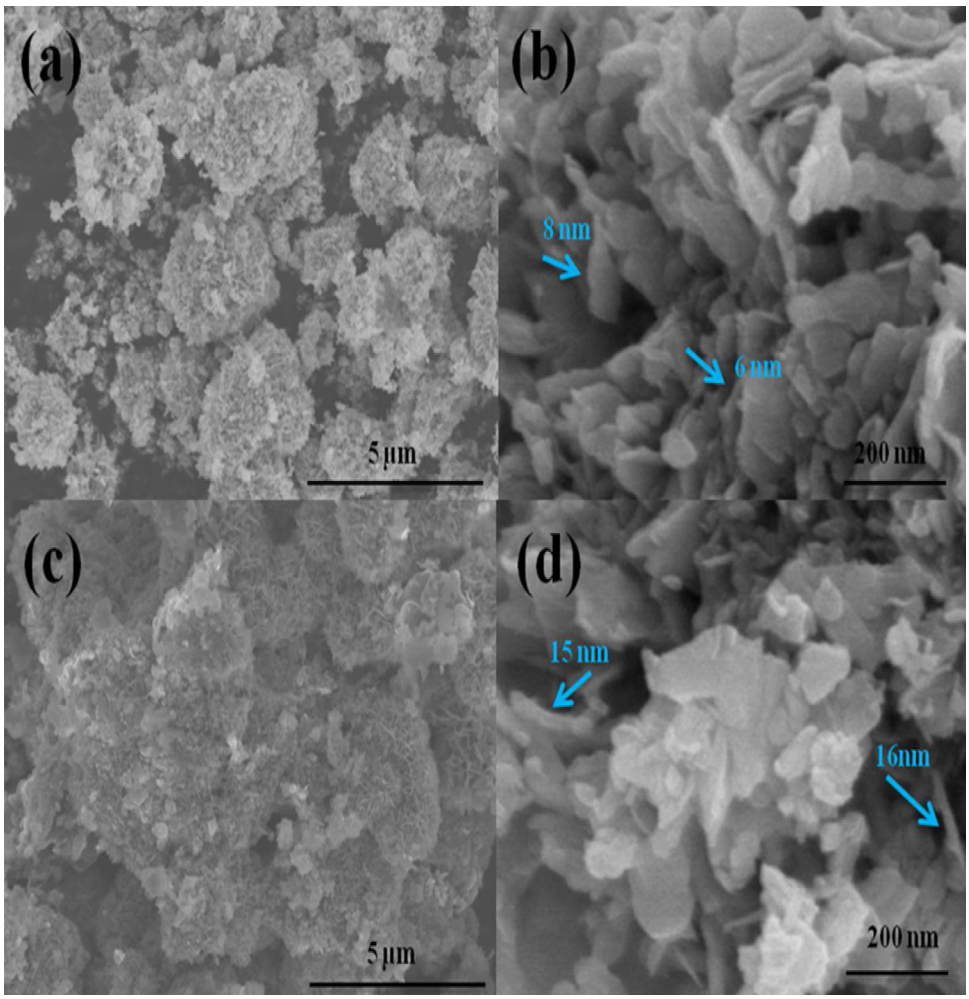


**Fig. 3.** SEM images of (a–b) $In_2S_3$ and (c–d) 7% BN/$In_2S_3$.

for optimizing the photoactivity of 2D–2D composites [8(e)–(g)]. When the weight ratio of BN is 7%, the sample exhibits the optimal photocatalytic activity, and the conversion of benzyl alcohol reaches to 60%. However, the conversion of benzyl alcohol is only 25% when pure $In_2S_3$ is used as a photocatalyst. Additionally, a control experiment using pure BN as a catalyst exhibits that there is no visible light activity, and benzaldehyde is not detected in the reaction system. It indicates that the primary photocatalytic ingredient is $In_2S_3$ in the BN/$In_2S_3$ composite. Moreover, photocatalytic activities of BN/$In_2S_3$ composites for selective oxidation of benzyl alcohol to benzaldehyde are all higher than that of the physical mixture of BN (7%) and $In_2S_3$ (93%). Furthermore, the mixed sample shows lower photocatalytic activity than that of pure $In_2S_3$. Therefore, it can be concluded that the improvement of the photocatalytic activity for BN/$In_2S_3$ composites is indeed attributed to the combination between BN nanosheets and $In_2S_3$.

Furthermore, based on the BET analysis, it is clear that there is a slight difference of the BET surface areas between these samples (BET surface area of 7% BN/$In_2S_3$ composite is a little lower than that of $In_2S_3$), demonstrating the enhancement of photocatalytic activity can not be attributed to the BET surface area. Therefore, the enhanced photocatalytic activity of BN/$In_2S_3$ composite can only be ascribed to the introduction of two-dimensional BN nanosheets.

Fig. 8 shows time-online profile of photocatalytic selective oxidation of benzyl alcohol over $In_2S_3$ and 7% BN/$In_2S_3$ composite. It is clear that compared with pure $In_2S_3$ sample, the superior photocatalytic performance of 7% BN/$In_2S_3$ composite is obvious. When the irradiation time is the same, the conversion of benzyl alcohol and the yield of benzaldehyde for the 7% BN/$In_2S_3$ composite are higher than those for $In_2S_3$ sample. It is proposed that the excellent photocatalytic performance of 7% BN/$In_2S_3$ composite may be attributed to highly efficient separation and transfer of photoexcited electron-hole pairs.

### 3.2.2. *Selective oxidation of different aromatic alcohols*

Based on the above results, it is clear that the 7% BN/$In_2S_3$ composite shows the best photocatalytic activity. Therefore, the 7% BN/$In_2S_3$ composite is chosen as the testing candidate to evaluate the photocatalytic performance for selective oxidation of other aromatic alcohols. Table 1 shows the photocatalytic performance of selective oxidation of a range of aromatic alcohols to corresponding aldehydes under visible light irradiation for 3 h. It can be seen that compared with pure $In_2S_3$ photocatalyst, the 7% BN/$In_2S_3$ composite exhibits higher photocatalytic activities for all testing reactions. It means that BN/$In_2S_3$ composite is able to perform as an efficient visible-light-driven photocatalyst for selective oxidation of aromatic alcohols to corresponding aldehydes. Furthermore, it is clear that the selectivity of different aromatic alcohols is not the same. The selectivity decreases as follows: p-methoxybenzyl alcohol > benzyl alcohol > p-chlorobenzyl alcohol > p-fluorobenzyl alcohol > p-nitrobenzyl alcohol > cinnamyl alcohol. It has been reported that the selectivity is directly proportional to the electronegativity of functional group [19,29]. It is known that electron donating ability of the functional group is as

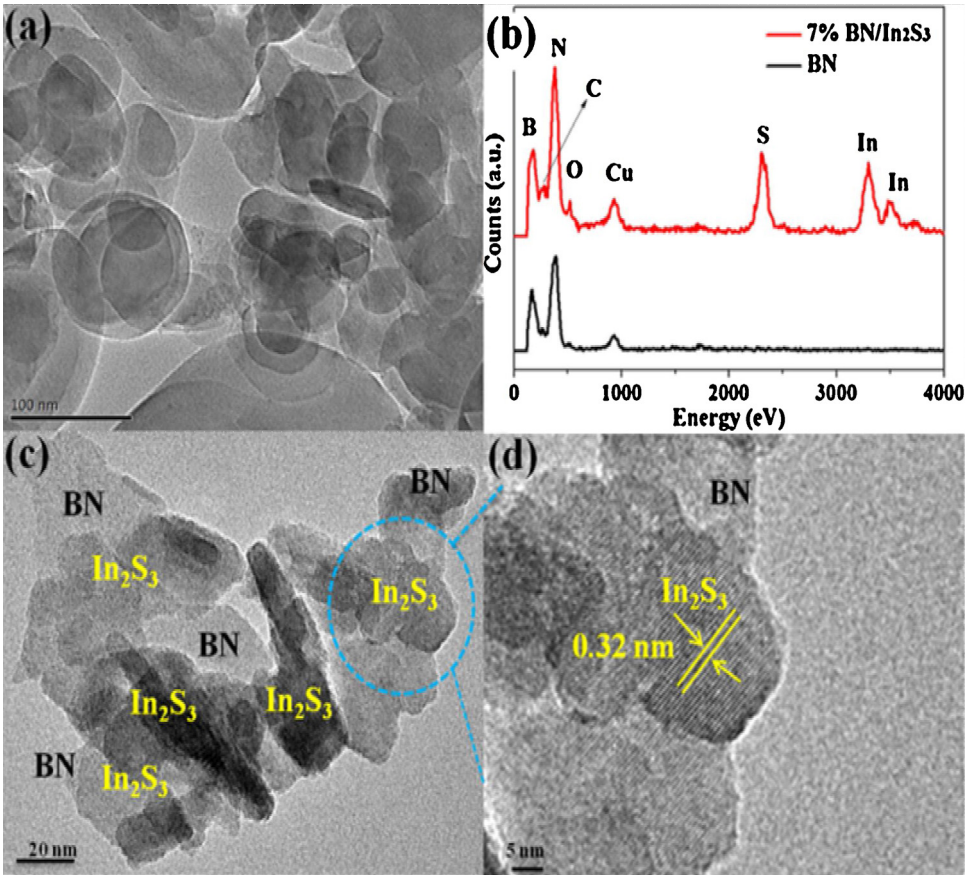


**Fig. 4.** (a) TEM image of BN nanosheets, (b) EDX patterns of $In_2S_3$ and 7% BN/$In_2S_3$, (c) TEM and (d) HR-TEM images of 7% BN/$In_2S_3$.

follows: $-OCH_3 > -H > -Cl > -F > -NO_2$. Therefore, the selectivity follows the above order. Moreover, the selectivity of the aromatic alcohols is relatively high except cinnamyl alcohol. This may be resulted from π-π conjugated effect, which is caused by the formation of benzene ring and C=C double bond, and then the π-π conjugated effect influences the oxidation process of cinnamyl alcohol [19]. The above results indicate that the BN/$In_2S_3$ composite photocatalyst is an excellent photocatalyst for selective oxidation of aromatic alcohols to corresponding aldehydes.

### 3.2.3. *Photocatalytic stability of BN/$In_2S_3$ composite*

In order to evaluate the photocatalytic stability of BN/$In_2S_3$ composite for photocatalytic oxidation of benzyl alcohol to benzaldehyde, the 7% BN/$In_2S_3$ composite is chosen to test by

**Table 1**
Photocatalytic performance for selective oxidation of a range of aromatic alcohols to corresponding aldehydes using pure $In_2S_3$ and 7% BN/$In_2S_3$ composite under visible light irradiation for 3 h (In Table, C, Y and S mean Conversion, Yield and Selectivity, respectively.)

| Entry | Substrate | Product | Pure In2S3 | | | 7% BN/In2S3 | | |
|---|---|---|---|---|---|---|---|---|
| | | | C% | Y% | S% | C% | Y% | S% |
| 1 | 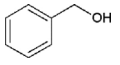 | 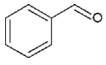 | 25 | 24 | 96 | 60 | 59 | 99 |
| 2 | 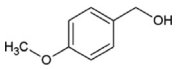 | 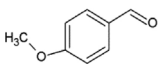 | 41 | 40 | 98 | 71 | 71 | 100 |
| 3 | 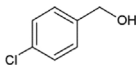 | 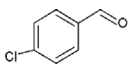 | 34 | 31 | 90 | 66 | 63 | 95 |
| 4 | 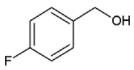 | 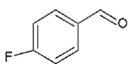 | 25 | 22 | 89 | 46 | 43 | 93 |
| 5 | 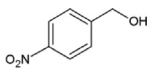 | 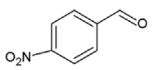 | 18 | 16 | 87 | 27 | 25 | 91 |
| 6 | 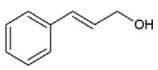 | 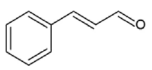 | 20 | 4 | 21 | 26 | 8 | 30 |

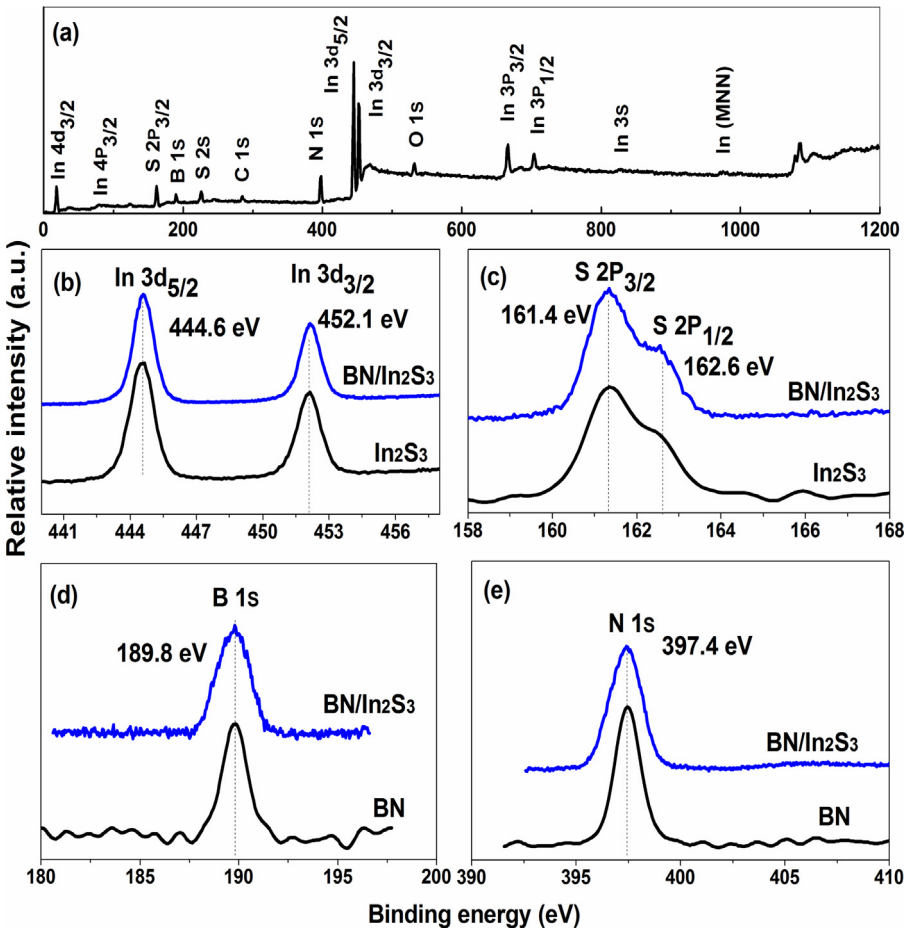


**Fig. 5.** (a) XPS survey spectra of 7% BN/$In_2S_3$ composite. High-resolution spectra of (b) In 3d and (c) S 2p for $In_2S_3$ and 7% BN/$In_2S_3$ samples, and (d) B 1s and (e) N 1s for BN and 7% BN/$In_2S_3$ samples.

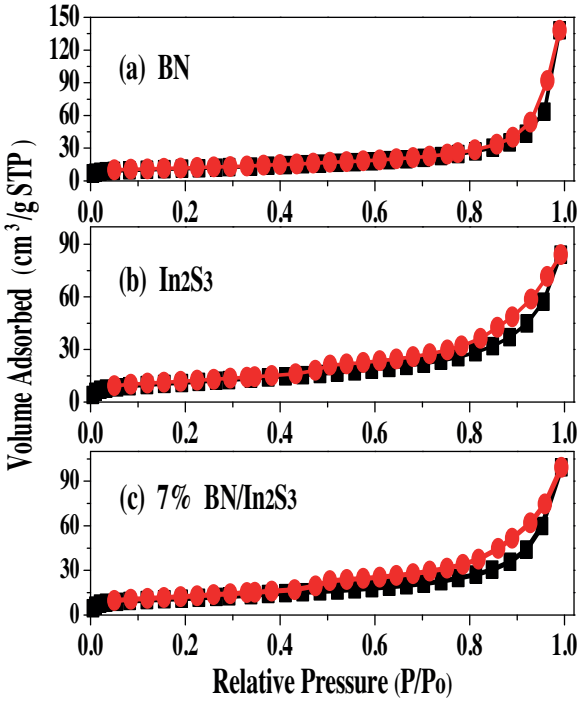


**Fig. 6.** Nitrogen adsorption–desorption isotherms of (a) BN, (b) $In_2S_3$ and (c) 7% BN/$In_2S_3$.

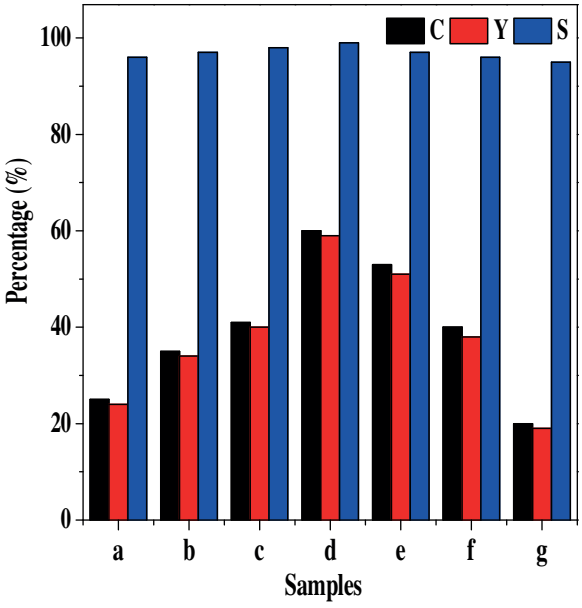


**Fig. 7.** Photocatalytic performance for selective oxidation of benzyl alcohol to benzaldehyde using $In_2S_3$ and BN/$In_2S_3$ composites under visible light irradiation for 3 h. (a) $In_2S_3$; (b) 3% BN/ $In_2S_3$; (c) 5% BN/ $In_2S_3$; (d) 7% BN/ $In_2S_3$; (e) 10% BN/ $In_2S_3$; (f) 20% BN/ $In_2S_3$; (g) 7% BN mixed with $In_2S_3$. (In Figs, C, Y and S mean Conversion, Yield and Selectivity, respectively. The black, red and blue bars represent Conversion, Yield and Selectivity, respectively.) (For interpretation of the references to colour in this figure legend, the reader is referred to the web version of this article.)

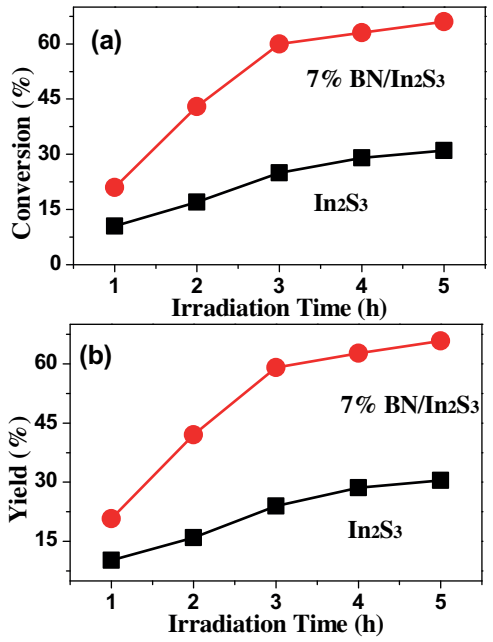


**Fig. 8.** Time-dependent profile for photocatalytic selective oxidation of benzyl alcohol to benzaldehyde (a, conversion; b, yield) over $In_2S_3$ and 7% BN/$In_2S_3$ composite under visible light irradiation.

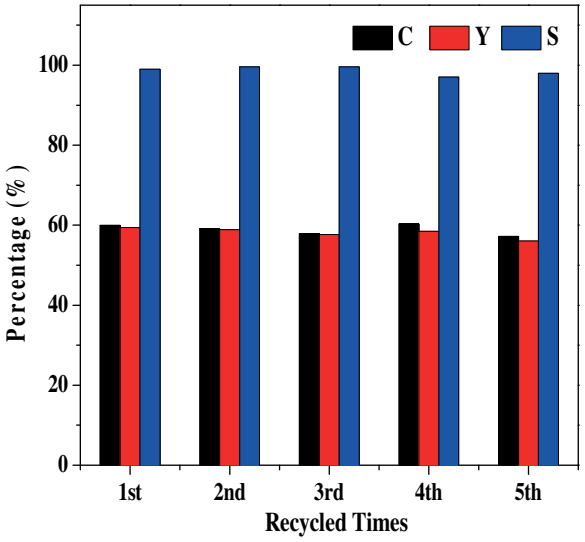


**Fig. 9.** Recycle experiment for photocatalytic oxidation of benzyl alcohol using 7% BN/$In_2S_3$ composite under visible light irradiation for 3 h. (In Figs, C, Y and S mean Conversion, Yield and Selectivity, respectively. The black, red and blue bars represent Conversion, Yield and Selectivity, respectively.) (For interpretation of the references to colour in this figure legend, the reader is referred to the web version of this article.)

successive cyclic experiments. As shown in Fig. 9, it is clear that the conversion and the selectivity have not obvious change after the catalyst is used for 5 times. It means that the photocatalytic activity of the sample is stable. Furthermore, from Fig. 10, it is clear that the used BN/$In_2S_3$ has identical XRD pattern with fresh BN/$In_2S_3$ composite. It is demonstrated that the bulk phase composition of the sample has no obvious change before and after photocatalytic reactions. Therefore, it is concluded that the BN/$In_2S_3$ composite is a stable visible-light-driven photocatalyst for selective oxidation of aromatic alcohols to corresponding aldehydes in the experimental condition.

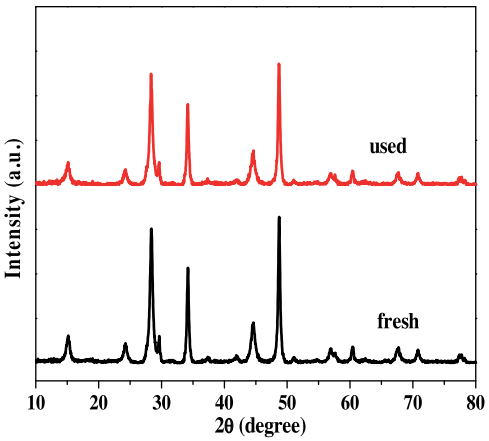


**Fig. 10.** XRD patterns of 7% BN/$In_2S_3$ photocatalyst before and after the photocatalytic reactions.

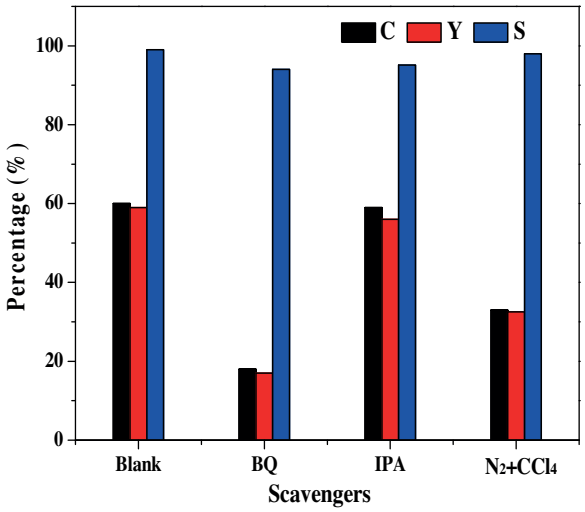


**Fig. 11.** Effects of a series of scavengers on the selective oxidation of benzyl alcohol (The dosage of scavengers = 0.1 mmol/L, Illumination time $t$ = 3 h). (In Figs, C, Y and S mean Conversion, Yield and Selectivity, respectively. The black, red and blue bars represent Conversion, Yield and Selectivity, respectively.) (For interpretation of the references to colour in this figure legend, the reader is referred to the web version of this article.)

### 3.3. Proposed photocatalytic mechanism

#### 3.3.1. Role of reactive species

As we all know, $O_2^-$, $h^+$ and•OH are the major reactive species for a photocatalytic oxidation reaction [16,18]. In order to investigate the free radicals in the reaction process of selective oxidation of aromatic alcohols to aromatic aldehydes, a series of control experiments were carried out. In the study, p-benzoquinone (BQ) was introduced as the quencher of $^{\bullet}O_2^-$ [30], isopropyl alcohol (IPA) was adopted to quench •OH [31], and carbon tetrachloride ($CCl_4$) was added into the reaction system as electrons quencher [32]. As shown in Fig. 11, when BQ is added into the reaction system, the yield of benzaldehyde is reduced obviously from 59% to 17%. A similar phenomenon is occurred when $CCl_4$ is added into the reaction system for trapping the photogenerated electrons. The above results indicate that $^{\bullet}O_2^-$ is an important active species in the photocatalytic reaction. Furthermore, the result also shows that when$^{\bullet}O_2^-$ or $O_2$ and $e^-$ are eliminated from the reaction system, BN/$In_2S_3$ composite still exhibits a certain amount of photocatalytic activity. It means that the photogenerated holes also participate

in the photocatalytic reaction. However, when IPA is added into reaction system, the yield of benzaldehyde is decreased negligibly. Therefore, it is concluded that $^{\bullet}O_2^-$ radicals and photogenerated holes play a decisive role in the photocatalytic oxidation of aromatic alcohols to aromatic aldehydes, while •OH radicals play a negligible role.

### 3.3.2. Validation of the reactive species

In order to determine the existence of the active species $^{\bullet}O_2^-$ and•OH, ESR technique was carried out in the reaction process [33]. The result is shown in Fig. 12. It is clear that the characteristic peaks of the DMPO-$^{\bullet}O_2^-$ adduct are observed for $In_2S_3$ and $BN/In_2S_3$ composite (Fig. 12a), but not found for DMPO methanol dispersion contained no photocatalyst (blank test for a reference). It demonstrates that $^{\bullet}O_2^-$ radicals are indeed produced on $In_2S_3$ and $BN/In_2S_3$ composite under visible light irradiation. It is worth noting that the peaks intensity of the DMPO-$^{\bullet}O_2^-$ adduct for 7% $BN/In_2S_3$ composite is higher than that for pure $In_2S_3$. That is to say, the amount of $^{\bullet}O_2^-$ radicals generated on the $BN/In_2S_3$ composite is higher than that of $In_2S_3$. The characteristic peaks of the DMPO-•OH adduct for $In_2S_3$ and $BN/In_2S_3$ composite could be observed from Fig. 12b. There are no signals of DMPO-•OH adduct for aqueous without photocatalyst. It indicates that •OH radicals are generated on $In_2S_3$ and $BN/In_2S_3$ composite after visible light irradiation. However, the peaks intensity is weak and difficult to be determined.

To further determine the•OH and $^{\bullet}O_2^-$ radicals generated in the photocatalytic process, TA-PL (Terephthalic acid-photoluminescence) [34] and NBT (Nitroblue tetrazolium) [35] experiments were performed. TA can react with free radical •OH to produce a highly fluorescence material, 2-hydroxyterephthalic acid. And its PL intensity is in proportion to the amount of •OH radicals. Thus, TA can be used for detecting whether •OH is produced in the reaction process [34]. As shown in Fig. 13a, it is clear that the amount of •OH produced on the surface of 7% $BN/In_2S_3$ composite is higher that of $In_2S_3$. However, the peak intensities of 2-hydroxyterephthalic acid formed on the surface of $In_2S_3$ and 7% $BN/In_2S_3$ are both weak, demonstrating the generated amount of•OH is little. It is consistent with the above results of DMPO-•OH measurement and the scavenger experiment. That is why the conversion of benzyl alcohol is not decreased obviously when IPA (•OH eliminating agent) was added into the reaction system. Nitroblue tetrazolium (NBT, $2.5 \times 10^{-5}$ mol/L, exhibiting an absorption maximum at 259 nm) was used to check whether there is $^{\bullet}O_2^-$ generated in the $BN/In_2S_3$ photocatalytic system [35]. From the Fig. 13b, it can be seen that the UV–vis absorption spectra at 259 nm for 7% $BN/In_2S_3$ with visible light irradiation and without visible light irradiation are both very low. However, in the dark condition, the decrease of the peak intension is attributed to the adsorption of negatively charged BN on the NBT, because in the aqueous solution NBT is in the form of cation ($NBT^{2+}$). In the visible light irradiation condition, the peak at 259 nm is reduced more than that of in the dark condition. It is confirmed that $^{\bullet}O_2^-$ radicals are indeed produced on $BN/In_2S_3$ in the reaction system.

### 3.3.3. Photoelectrochemical properties

Photoelectrochemical experiments were carried out to explore the electronic interaction between BN and $In_2S_3$. Fig. 14a displays the transient photocurrent response of pure $In_2S_3$ and 7% $BN/In_2S_3$ composite under intermittent visible light irradiation. It is clear that the fast photocurrent response for each switch-on and switch-off event in both electrodes is observed. Notably, it can be seen that compared with pure $In_2S_3$, the $BN/In_2S_3$ composite enhances the photocurrent density significantly. Because the photocurrent is mainly produced by the diffusion of photoexcited electrons; simultaneously, the photoexcited holes are captured by hole-accepter in the electrolyte [36]. Therefore, the enhanced photocurrent density for the 7% $BN/In_2S_3$ means that the photoexcitrd carriers are separated effectively, and photoexcited electro-hole pairs have a long lifetime compared with pure $In_2S_3$. Electrochemical impedance spectroscopy (EIS) was further performed to investigate the separation efficiency of the photoinduced charge carriers [37]. As displayed in Fig. 14b, only one arc/semicircle is observed at high frequency on the EIS spectrum, indicating that only surface charge-transfer is involved in the photocatalytic reaction system [38]. The smaller arc radius of the EIS Nyquist plot corresponds to the more effective separation of the photoinduced electron-hole and the faster interfacial charger transfer to the electron donor/acceptor. Consequently, compared with the pure $In_2S_3$, the smaller arc radius of 7% $BN/In_2S_3$ composite suggests that the separation efficiency of the photoinduced electron-hole and the charge transfer over 7% $BN/In_2S_3$ composite are superior to those over the pure $In_2S_3$. These photoelectro-chemical results are in agreement with that of photocatalytic activity test.

To study the origin of enhanced photoelectrochemical performances of the $BN/In_2S_3$ composite, open circuit photovoltage decay (OCPV) tests were carried out (Fig. 14c). OCPV technique can be served as a powerful tool in studying the lifetime of photoelectrons and the recombination rate of the photogenerated electron-hole by turning off light first at a steady state and monitor the photovoltage ($V_{OC}$) decay with time [38]. The potential-dependent photoelectron lifetime ($\tau$) can be calculated by the following equation [39]: $\tau = (k_BT/e)(dV_{OC}/dt)^{-1}$. In this equation, $k_B$, T, e and t are the Boltzmann's constant ($1.3806 \times 10^{-23}$ J/K), the temperature (298.15 K), the charge of one electron ($1.602 \times 10^{-19}$ C) and time, respectively. Fig. 14d shows the calculated $\tau$ as a function of $V_{OC}$. It is clear that $BN/In_2S_3$ composite manifests remarkably prolonged electron lifetime in comparison with the pure $In_2S_3$, thus contributing to the significantly enhanced photoelectrochemical and photocatalytic performances.

### 3.3.4. Photoluminescence emission spectra

The photoexcited electron-hole lifetime of $BN/In_2S_3$ sample is further confirmed by the photoluminescence (PL) measurement. It has been well-established that PL technique can be applied to assess the recombination rate of the photoexcited electron-hole charge carriers [40]. Generally, a lower PL intensity indicates a lower recombination rate of the photoexcited electron-hole and vice versa. Fig. 15 shows the PL spectra of $In_2S_3$ and $BN/In_2S_3$ composite. It is clear to observe that 7% $BN/In_2S_3$ composite displays a lower PL intensity than that of pure $In_2S_3$, suggesting that the recombination rate of the photoexcited electron-hole is efficiently restrained after the combination of $In_2S_3$ with BN nanosheets. The above results are consistent with the photoelectrochemical analysis and also in accordance with the photocatalytic activity test.

### 3.3.5. Reaction mechanisms

According to the above experimental results and analysis, the reaction mechanism for photocatalytic selective oxidation of aromatic alcohols to corresponding aromatic aldehydes over $BN/In_2S_3$ composite is illustrated in Fig. 16. When $BN/In_2S_3$ composite is irradiated by visible light, the photoexcited electrons and holes are produced in the conduction band and the valence band of $In_2S_3$, respectively. The photoexcited holes are transferred rapidly due to the electrostatic attraction between the holes and the negatively charged BN, and then participate in photocatalytic reaction. More importantly, it is favorable for efficient separation of photoexcited electron-hole pairs and prolonging electrons lifetime. Subsequently, the photoexcited electrons will be captured by the dissolved $O_2$ to generate $^{\bullet}O_2^-$, which directly participate in the

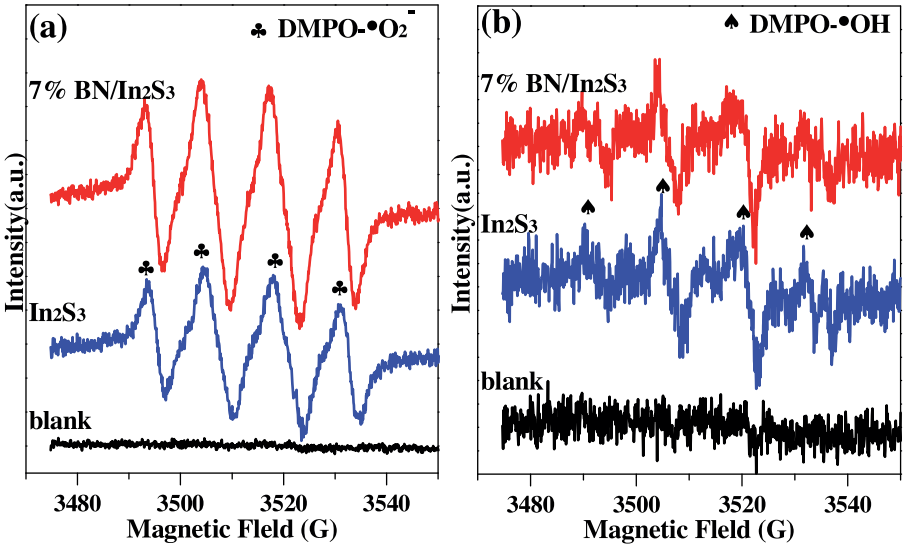


**Fig. 12.** ESR signals of (a) the DMPO-•$O_2^-$ and (b) DMPO-•OH with irradiation for 60 s in methanol and aqueous dispersion contained no photocatalyst (blank) and photocatalysts ($In_2S_3$ or the 7% BN/$In_2S_3$ composite), respectively.

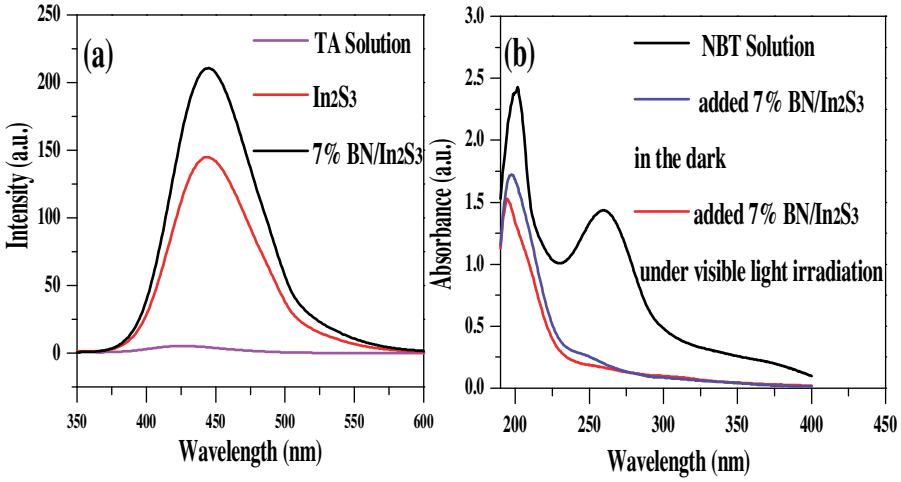


**Fig. 13.** (a) Photoluminescence (PL) emission spectra of the TA solution contained no photocatalyst (blank), $In_2S_3$ and 7% BN/$In_2S_3$ composite under visible light irradiation. (b) The absorbance of NBT solution under different conditions.

oxidation reaction. Therefore, the BN/$In_2S_3$ composite exhibits the enhanced photocatalytic activities compared with pure $In_2S_3$.

### *3.4. Selective oxidation of benzyl alcohol for other BN/metal sulfide*

To illustrate the role of BN nanosheet for improving photocatalytic activity in BN/metal sulfide composite, other three BN/metal sulfide composites (BN/$ZnIn_2S_4$, BN/$Cd_xZn_{1-x}S$ and BN/CdS) were also investigated. As shown in Fig. 17, XRD analysis revealed that the as-synthesized metal sulfides are well crystallized. The as-prepared $ZnIn_2S_4$, $Cd_xZn_{1-x}S$ and CdS can be well indexed to the hexagonal structures of $ZnIn_2S_4$ (JCPDS No. 65-2023) [41], $Cd_xZn_{1-x}S$ ($Cd_{0.75}Zn_{0.25}S$) [42] and CdS (JCPDS No. 41-1049) [43], respectively. For BN/metal sulfide composites, the XRD patterns are similar to the corresponding pure-phase metal sulfide, except one diffraction peak at 26.9°, which can be indexed to the main characteristic peak of hexagonal-BN. Furthermore, it is clear that BN/metal sulfide composites exhibit a stronger diffraction peak at 26.9° than the pure-phase of metal sulfides because two peaks overlap.

Further investigation was carried out by SEM to reveal the morphology and microscopic structure of these samples. It can be seen that $ZnIn_2S_4$ is consisted of numerous microspheres with diameter of 1.5–6 μm (Fig. 18a), and the marigold-like spherical structure is further composed of numerous nanosheets. It is in accordance with the previous reports. For $Cd_{0.75}Zn_{0.25}S$ sample, the dendrite structure can be clearly observed from Fig. 18c, which displays a multilevel generation with a long main trunk of 2–6 μm and short side branches of 0.3–2 μm. The as-prepared CdS has spherical-like morphology resulting from the accumulation of small CdS nanoparticles with diameter of 60–200 nm (Fig. 18e). Fig. 18(b, d and f) exhibit the SEM images of BN/metal sulfide composites. It is clear that although BN nanosheets are introduced in the samples, the

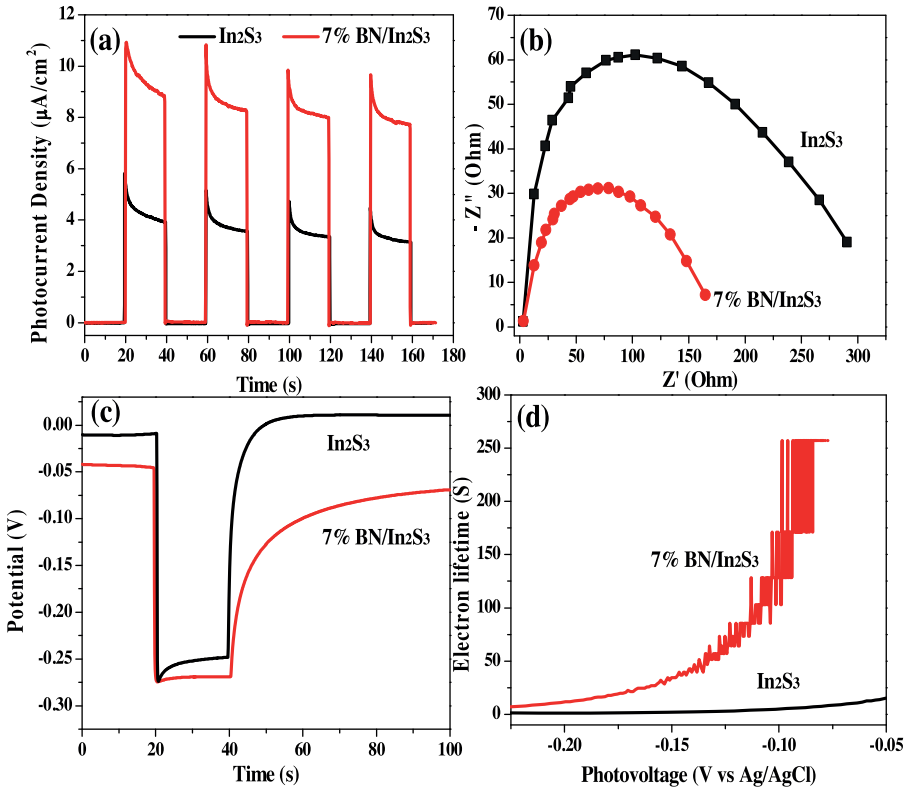


**Fig. 14.** (a) Transient photocurrent density of $In_2S_3$ and 7% BN/$In_2S_3$ electrodes in 0.1 M $Na_2SO_4$ solution without bias versus Ag/AgCl under visible light irradiation. (b) EIS Nyquist plots of $In_2S_3$ and 7% BN/$In_2S_3$ composite in 0.1 M KCl solution containing 0.1 M $K_3[Fe(CN)_6]$/ $K_4[Fe(CN)_6]$. (c) Illuminated open circuit potential of $In_2S_3$ and 7% BN/$In_2S_3$ electrodes in 0.1 M $Na_2SO_4$ solution without bias versus Ag/AgCl. (d) Electron lifetime determined from the decay of open circuit potential in dark.

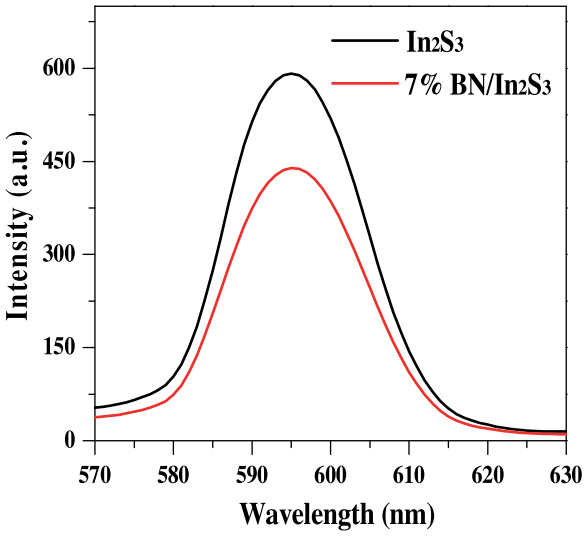


**Fig. 15.** PL spectra of pure $In_2S_3$ and 7% BN/$In_2S_3$ composite.

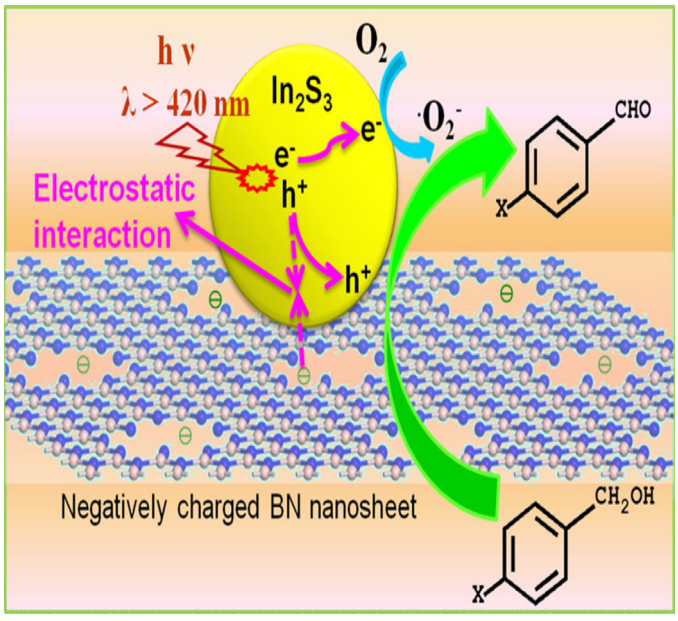


**Fig. 16.** Proposed reaction mechanism for photocatalytic selective oxidation of benzyl alcohol over BN/$In_2S_3$ composite.

morphologies of these metal sulfides have no dramatical change except some flakes.

The photocatalytic activities of $ZnIn_2S_4$, BN/$ZnIn_2S_4$, $Cd_{0.75}Zn_{0.25}S$, BN/ $Cd_{0.75}Zn_{0.25}S$, CdS and BN/CdS for selective oxidation of benzyl alcohol to benzaldehyde are shown in Fig. 19. It can be seen that compared with pure metal sulfides, the photocatalytic activities (conversions of benzyl alcohol and yields of benzaldehyde) of BN/metal sulfides are all remarkably enhanced. It is demonstrated that an improvement of the photocatalytic activities should be ascribed to the introduction of negatively charged 2D BN nanosheets. Therefore, it is concluded that metal sulfides coupled with BN is a versatile method for improving their photocatalytic performance.

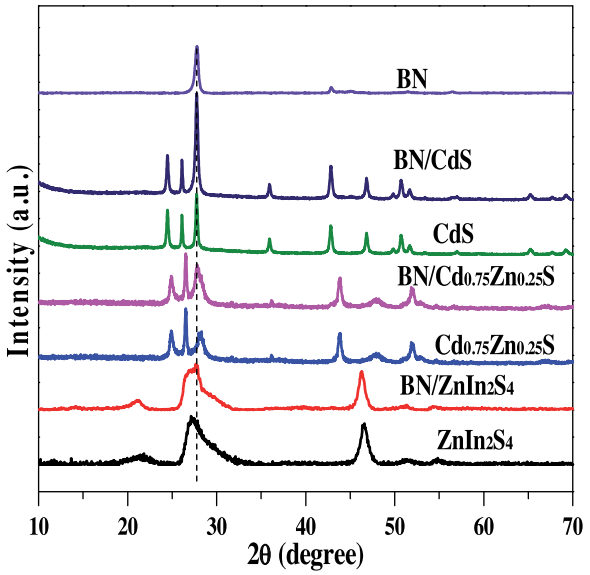


**Fig. 17.** XRD patterns of the metal sulfides, BN, and BN/metal sulfide composites.

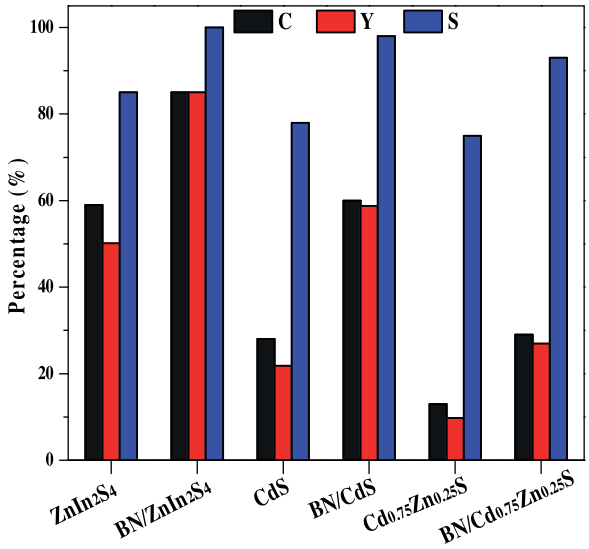


**Fig. 19.** Photocatalytic performance for selective oxidation of benzyl alcohol to corresponding benzaldehyde using different photocatalysts under visible light irradiation for 3 h. (In Figs, C, Y and S mean Conversion, Yield and Selectivity, respectively. The black, red and blue bars represent Conversion, Yield and Selectivity, respectively.) (For interpretation of the references to colour in this figure legend, the reader is referred to the web version of this article.)

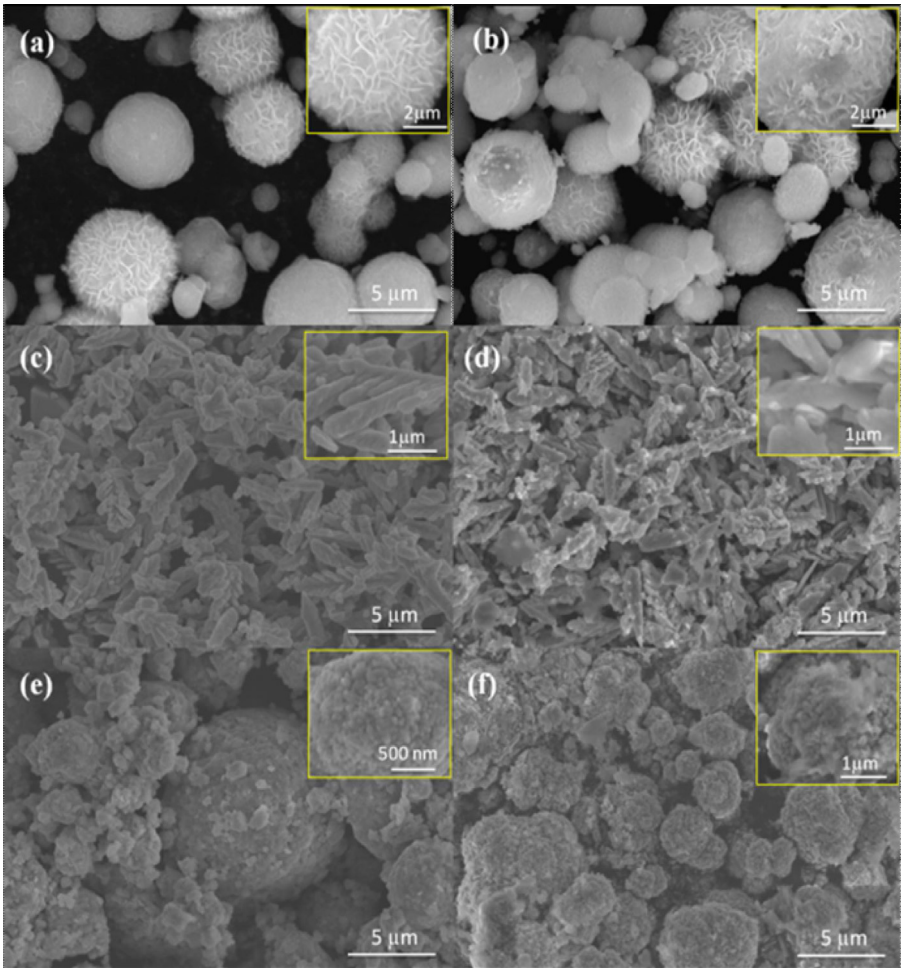


**Fig. 18.** SEM images of (a) $ZnIn_2S_4$, (b) BN/$ZnIn_2S_4$, (c) $Cd_{0.75}Zn_{0.25}S$, (d) BN/$Cd_{0.75}Zn_{0.25}S$, (e) CdS and (f) BN/CdS with corresponding high-magnified images in the inset.

## 4. Conclusions

BN/$In_2S_3$ composites with different mass ratio were synthesized by a one-step hydrothermal method. The as-prepared BN/$In_2S_3$ composites can be used for selective oxidation of aromatic alcohols to aromatic aldehydes under visible light illumination. 7% BN/$In_2S_3$ composite displays the highest photocatalytic activity. The significantly enhanced photocatalytic activity of BN/$In_2S_3$ is attributed to the introduction of BN nanosheets, which can enhance the separation and transfer efficiencies of the photogenerated electron-hole charge carriers. This versatile approach can be applied in synthesis of other BN/metal sulfide (such as CdS, $Cd_xZn_{1-x}S$ and $ZnIn_2S_4$) composites with high photocatalytic performance.

## Acknowledgements

This study was supported by the Natural Science Foundation of China (NSFC, grant Nos. 51472005, 51172086, 51272081,21473066 and 21103060) and the Natural Science Foundation of Anhui Province (grant no. 1408085QB38).

## References

[1] (a) A. Baiker, T. Mallat, Chem. Rev. 104 (2004) 3037–3058.
[2] (a) M. Zhang, Q. Wang, C. Chen, L. Zang, W. Ma, J. Zhao, Angew. Chem. 121 (2009) 6197–6200;
(b) P.L. Anelli, C. Biffi, F. Montanari, S. Quici, J. Org. Chem. 52 (1987) 2559–2562;
(c) S. Patel, B.K. Mishra, J. Org. Chem. 71 (2006) 6759–6766.
[3] T. Mallat, A. Baiker, Chem. Rev. 104 (2004) 3037–3058.
[4] (a) A. Fujishima, K. Honda, Nature 238 (1972) 37–38;
(b) D.Y.C. Leung, X.L. Fu, C.F. Wang, M. Ni, M.K. Leung, X.X. Wang, X.Z. Fu, ChemSusChem 3 (2010) 681–694.
[5] (a) X. Li, J. Yu, J. Low, Y. Fang, J. Xiao, X. Chen, J. Mater. Chem. A 3 (2015) 2485–2534.
[6] (a) O. Legrini, E. Oliveros, A.M. Braun, Chem. Rev. 93 (1993) 671–698;
(b) Y. Zhang, Z. Tang, X. Fu, Y. Xu, Appl. Catal. B Environ. 106 (2011) 445–452.
[7] (a) Y. Shiraishi, T. Hirai, J. Photoch. Photobio. C 9 (2008) 157–170;
(b) M.Q. Yang, N. Zhang, Y.J. Xu, ACS Appl. Mater. Interfaces 5 (2013) 1156–1164.
[8] (a) H. Cheng, K. Fuku, Y. Kuwahara, K. Mori, H. Yamashita, J. Mater. Chem. A 3 (2015) 5244–5258;
(b) H. Tong, S.X. Ouyang, Y.P. Bi, N. Umezawa, M. Oshikir, J.H. i Ye, Adv. Mater. 24 (2012) 229–251;
(c) W. Tu, Y. Zhou, Z. Zou, Adv. Funct. Mater. 23 (2013) 4996–5008;
(d) G. Dong, W. Ho, Y. Li, L. Zhang, Appl. Catal. B Environ. 174–175 (2015) 477–485;
(e) L. Ge, C. Han, X. Xiao, L. Guo, Int. J. Hydrogen Energy 38 (2013) 6960–6969;
(f) Q.J. Xiang, J.G. Yu, M. Jaroniec, J. Phys. Chem. C 115 (2011) 7355–7363.
[9] (a) G. Liu, H.G. Yang, J. Pan, Y.Q. Yang, G.Q. Lu, H.M. Cheng, Chem. Rev. 114 (2014) 9559–9612;
(b) T. Kamegawa, Y. Ishiguro, H. Seto, H. Yamashita, J. Mater. Chem. A 3 (2015) 2323–2330.
[10] (a) S. Yurdakal, G. Palmisano, V. Loddo, V. Augugliaro, L. Palmisano, J. Am. Chem. Soc. 130 (2008) 1568–1569.
[11] J. Fan, Y. Dai, Y. Li, N. Zheng, J. Guo, X. Yan, G.D. Stucky, J. Am. Chem. Soc. 131 (2009) 15568–15569.
[12] D.I. Enache, J.K. Edwards, P. Landon, B. Solsona-Espriu, A.F. Carley, A.A. Herzing, M. Watanabe, C.J. Kiely, D.W. Knight, G.J. Hutchings, Science 311 (2006) 362–365.
[13] (a) Y. Zhang, Z. Tang, X. Fu, Y. Xu, ACS Nano 5 (2011) 7426–7435.
[14] A. Tanaka, K. Hashimoto, H. Kominami, J. Am. Chem. Soc. 134 (2012) 14526–14533.
[15] J. Xu, L. Luo, G. Xiao, Z. Zhang, H. Lin, X. Wang, J. Long, ACS Catal. 4 (2014) 3302–3306.
[16] B. Long, Z. Ding, X. Wang, ChemSusChem 6 (2013) 2074–2078.
[17] (a) Y. Hu, X. Gao, L. Yu, Y. Wang, J. Ning, S. Xu, X.W. Lou, Angew. Chem. Int. Ed. 125 (2013) 5746–5749.
[18] (a) Z. Chen, J. Xu, Z. Ren, Y. He, G. Xiao, Catal. Commun. 41 (2013) 83–86.
[19] (a) M. Xie, D. Xia, S. Meng, X. Fu, S. Chen, Chem. Eng. J. 245 (2014) 107–116.
[20] (a) W. Yang, L. Zhang, Y. Hu, Y. Zhong, H.B. Wu, X.W. Lou, Angew. Chem. Int. Ed. 51 (2012) 11501–11504;
(b) X. Ye, Y. Cui, X. Qiu, X. Wang, Appl. Catal. B Environ. 152–153 (2014) 383–389;
(c) F.Z. Su, S.C. Mathew, G. Lipner, X.Z. Fu, M. Antonietti, S. Blechert, X.C. Wang, J. Am. Chem. Soc. 132 (2010) 16299–16301;
(d) N. Zhang, Y. Zhang, X. Pan, X. Fu, S. Liu, Y. Xu, J. Phys. Chem. C 115 (2011) 23501–23511;
(e) X. Gao, H.B. Wu, L. Zheng, Y. Zhong, Y. Hu, X.W. Lou, Angew. Chem. 126 (2014) 6027–6031.
[21] X. Li, B. Weng, N. Zhang, Y. Xu, RSC Adv. 4 (2014) 64484–64493.
[22] (a) Q. Lin, L. Li, S. Liang, M. Liu, J. Bi, L. Wu, Appl. Catal. B Environ. 163 (2015) 135–142;
(b) D. Golberg, Y. Bando, Y. Huang, T. Terao, M. Mitome, C. Tang, C. Zhi, ACS Nano 4 (2010) 2979–2993.
[23] X. Fu, Y. Hu, Y. Yang, W. Liu, S. Chen, J. Hazard. Mater. 244–245 (2013) 102–110.
[24] (a) R.F. Liu, C. Cheng, Phys. Rev. B 765 (2007) 014405;
(b) A. Katzir, J.T. Suss, A. Zunge, A. r Halperin, Phys. Rev. B 11 (1975) 2370–2377;
(c) L.C. Yin, H.M. Cheng, R. Saito, Phys. Rev. B 81 (2010) 153407;
(d) Y. Ide, F. Liu, J. Zhang, N. Kawamoto, K. Komaguchi, Y. Bando, D. Golberg, J. Mater. Chem. 2 (2014) 4150–4156.
[25] (a) M. Zhang, C. Chen, W. Ma, J. Zhao, Angew. Chem. Int. Ed. 47 (2008) 9730–9733.
[26] Q. Zhang, L. Gao, J. Guo, Appl. Catal. B: Environ. 26 (2000) 207–215.
[27] (a) M.A. Butler, J. Appl. Phys. 48 (1977) 1914–1920.
[28] (a) Y. Liu, H. Xu, Y. Qian, Cryst. Growth Des. 6 (2006) 1304–1307;
(b) L. Liu, H. Liu, H.Z. Kou, Y. Wang, Z. Zhou, M. Ren, M. Ge, X. He, Cryst. Growth Des. 9 (2009) 113–117.
[29] (a) T. Punniyamurthy, S. Velusamy, J. Iqbal, Chem. Rev. 105 (2005) 2329–2363.
[30] R. Palominos, J. Freer, M.A. Mondaca, H.D. Mansilla, J. Photochem. Photobiol. A 193 (2008) 139–145.
[31] (a) M. Sadakane, K. Sasaki, H. Kunioku, B. Ohtani, W. Ueda, R. Abe, Chem. Commun. 48 (2008) 6552–6554.
[32] X. Xiao, J. Jiang, L. Zhang, Appl. Catal. B: Environ. 142–143 (2013) 487–493.
[33] (a) C.C. Chen, P.X. Lei, H.W. Ji, W.H. Ma, J.C. Zhao, Environ. Sci. Technol. 38 (2004) 329–337.
[34] (a) K. Ishibashi, A. Fujishima, T. Watanabe, K. Hashimato, J. Photochem. Photobiol. A 134 (2000) 139–142.
[35] (a) L. Ye, J. Liu, Z. Jiang, T. Peng, L. Zan, Appl. Catal. B Environ. 142–143 (2013) 1–7;
(b) B.H.J. Bielski, H.W. Richter, J. Am. Chem. Soc. 99 (1977) 3019–3023.
[36] (a) H.W. Han, X.Z. Zhao, J. Liu, J. Electrochem. Soc. 152 (2005) A164–A166.
[37] (a) N. Li, G. Liu, C. Zhen, F. Li, L.L. Zhang, H.M. Cheng, Adv. Funct. Mater. 21 (2011) 1717–1722;
(b) H.B. Fu, T.G. Xu, S.B. Zhu, Y.F. Zhu, Environ. Sci. Technol. 42 (2008) 8064–8069.
[38] (a) F.X. Xiao, S.F. Huang, H.B. Tao, J. Miao, H.B. Yang, B. Liu, Nanoscale 6 (2014) 14950–14961.
[39] B.H. Meekins, P.V. Kamat, ACS Nano 3 (2009) 3437–3446.
[40] (a) J. Yang, H. Yan, X. Wang, F. Wen, Z. Wang, D. Fan, J. Shi, C. Li, J. Catal. 290 (2012) 151–157.
[41] (a) Z. Chen, D. Li, W. Zhang, C. Chen, W. Li, M. Sun, Y. He, X. Fu, Inorg. Chem. 47 (2008) 9766–9772;
(b) G. Chen, N. Ding, F. Li, Y. Fan, Y. Luo, D. Li, Q. Meng, Appl. Catal. B Environ. 160–161 (2014) 614–620.
[42] W. Li, D. Li, S. Meng, W. Chen, X. Fu, Y. Shao, Environ. Sci. Technol. 45 (2011) 2987–2993.
[43] (a) J. Jin, J. Yu, G. Liu, P.K. Wong, J. Mater. Chem. A 1 (2013) 10927–10934.